International Journal of Solids and Structures 51 (2014) 3762–3775

Contents lists available at ScienceDirect

International Journal of Solids and Structures

journal homepage: www.elsevier.com/locate/ijsolstr

Prediction of stress–strain and fracture behaviour of an 8-Harness satin weave ceramic matrix composite

Daxu Zhang [1], D.R. Hayhurst *

School of Mechanical, Aerospace and Civil Engineering, George Begg Building C004, The University of Manchester, Sackville Street, Manchester M13 9PL, UK

ARTICLE INFO

Article history:
Received 27 September 2013
Received in revised form 14 June 2014
Available online 27 July 2014

Keywords:
Ceramic matrix composites
Tows
Unit cell
8-Harness woven composite
Stress–strain response
Damage mechanisms
Orthotropic material

ABSTRACT

A computationally economic finite-element-based approach has been developed to predict the stress–strain and fracture behaviour of an 8-Harness satin woven ceramic matrix composite with strain-induced damage. The finite element analysis utilises a solid element to model the behaviour of the homogenised orthotropic uni-directional tow and its matrix. The underpinning models of the tow and matrix, (Tang et al., 2009) capture the physics of the interactions between fibres and matrix; and, in this way, permit modelling that bridges the length scales of the fibres and full-scale components. The non-linear multi-axial stress–strain behaviour of the composite has been discretised by multi-linear elastic curves; and the latter has been used as input to a user defined subroutine, UMAT, in the commercial finite element package, ABAQUS. A partial unit cell model has been constructed of the 8-Harness satin weave composite of carbon fibres embedded in an amorphous carbon matrix, HITCO C/C. Predictions of the global stress–strain curve, which include the effects of fibre waviness, have been made for two failure modes: the first by deformation localisation, and the second by dynamic tow failure on fibre fracture, triggered by instantaneous pull-out deactivation. Comparisons have been made between the predictions and experimental data that exhibit two classes of fracture behaviour: brittle and quasi-ductile. The predicted results, both with and without tow waviness, compare well with the experimental data; however, the predictions for waviness are slightly better. The two extremes of experimental behaviour have been found to correspond with the two tow fracture criteria modelled.

© 2014 The Authors. Published by Elsevier Ltd. This is an open access article under the CC BY license (http://creativecommons.org/licenses/by/3.0/).

1. Introduction

The low density and good high temperature mechanical and thermal properties of ceramic matrix composites (CMCs) render them ideal for use in rocket nozzles; thermal protection systems; and gas turbine engines (Marshall and Cox, 2008). In addition, they provide the potential to operate engineering components at higher operating temperatures, and hence achieve improved thermal efficiencies and achieve lower emissions (Evans and Naslain, 1995). To enable the use of CMCs in engineering components and structures it is necessary to simulate the material, and the component response at the detailed design and manufacturing stages (McGlockton et al., 2003). The complex spatial topology of the woven tows (Rinaldi et al., 2012; Blacklock et al., 2012) and the associated interactive damage mechanisms of the fibres, matrices, and CMC tows, necessitate the use of accurate and computationally fast methods of analysis (Zhang and Hayhurst, 2010).

In recent decades, the behaviour of woven composites has been investigated using the concept of a unit cell (representative volume element, RVE) that represents the basic repeatable element of the composite. The driver has been to predict the behaviour of the RVE from knowledge of the constituent materials properties. Three dimensional finite element models of RVEs have been used, at the meso-scale, in which heterogeneous fibre tows are assumed to be homogeneous. Zhang and Harding (1990) used finite elements and the principle of strain energy equivalence to investigate a one-ply plain weave composite. Incremental advancements were subsequently made by the following: Dasgupta and Agarwal (1992), Woo and Whitcomb (1997), Kuhn and Charalambides (1998), Tan et al. (1999), Ismar et al. (2000) and Sheikh et al. (2001); with Tan et al. (1997) and Onal and Adanur (2007) providing explicit accounts of developments. A disadvantage of the approach employed by these researchers is that they used very large numbers of finite elements to model the details of the geometry of the constituent elements and their interfaces, with the upshot that long and expensive computational time were necessary. It is therefore likely that these

* Corresponding author. Tel.: +44 1613063818.
E-mail address: d.r.hayhurst@manchester.ac.uk (D.R. Hayhurst).
[1] Current Address: School of Naval Architecture, Ocean and Civil Engineering, Shanghai Jiao Tong University, 800 Dongchuan Road, Shanghai 200240, China.

http://dx.doi.org/10.1016/j.ijsolstr.2014.07.010
0020-7683/© 2014 The Authors. Published by Elsevier Ltd.
This is an open access article under the CC BY license (http://creativecommons.org/licenses/by/3.0/).

techniques will be prohibitively expensive to use in the analysis of engineering components and structures.

Constitutive equations have been developed by Burr et al. (1997) that model CMCs matrix cracking, interface debonding, sliding, fibre failure, and pull-out. The approach, based within a Continuum Damage Mechanics framework, uses an energy formulation and state variables that relate to micro-mechanisms of damage and fracture. Their paper lacks clarity on how the finite element-based computations were done, and on how numerical stability was preserved during damage growth and unloading. Also, Lubineau and Ladevèze (2008) developed a mesoscale damage mechanic model for intra-laminar composite behaviour. Softening was sequentially triggered by a number of non-linear damage variables that each introduced its own plasticity, with localisation and mesh dependence cited as problems. They used a delay effect framework to avoid numerical problems associated with unloading and localisation. The techniques of Burr et al. (1997) and Lubineau and Ladevèze (2008) were developed for uni-directional straight fibres; and not the complex 8-satin woven material to be considered here.

Other finite element techniques have been employed to overcome these difficulties, Tanov and Tabiei (2001) analysed plain weave fabric composites by homogenising a model of an entire unit cell. Xu et al. (1995) have used the Binary Technique, which models the material as two virtual components: a 1-D truss element and a 3-D solid element. However, the Binary Technique requires accurate calibration of the mechanical and thermal properties of the two virtual components. Despite its success for polymer composites it has not been widely used for CMCs, however the work of Flores et al. (2010) is an exception. They used a Drucker–Prager plasticity model to generate a "blanket" overview of fibre failure and pull-out; however, the construct was deficient in that it was not possible to follow damage evolution and composite failure in the chosen structure, i.e. a tension panel containing a central circular hole. Hence the objective of aiding the physical interpretation of the experimental results was not fully realised.

Rather than employing the binary method, Zhang and Hayhurst (2009) have used a simpler and more accurate finite element approach of modelling the tow material as an orthotropic medium. They used this technique to model the behaviour of a Nicalon fibre – CAS matrix 0°/90° composite, and a C fibre – SiC/C matrix plain weave composite DLR-XT. Both materials were modelled under mechanical loading (Zhang and Hayhurst, 2010), and under thermo-mechanical conditions for the degradation of transverse thermal conductivity behaviour (Zhang and Hayhurst, 2011); and Hayhurst (2013) has also addressed the issue of thermo-mechanical coupling (2013). Both the predicted mechanical and the thermal responses of these materials have been compared with the results of experiments by Sheikh et al. (2009) and close agreement has been achieved.

The present paper addresses the extension of the approach established by Zhang and Hayhurst (2010) for mechanical loading of 0°/90° and plain weave composites to the more complex 8-Harness weave structure of a carbon fibre – amorphous carbon matrix 8-Harness satin weave HITCO composite. The latter material has also been tested by Sheikh et al. (2009), and was shown to exhibit uncharacteristic stress–strain and thermal degradation response. The challenge addressed in this paper is to predict and understand the behaviour of the material in detail.

The approach adopted in this paper is the finite element technique of Zhang and Hayhurst (2010), which emphasises the effects of strain-induced damage modes and their interactions on the mechanical behaviour. Non-linear tow material properties are modelled by multi-linear elastic discretisation. The method adopted by Tang et al. (2009) of modelling the composite using assemblies of tows, i.e. a collection of thousands of fibres embedded in at least one matrix, is embodied in the approach; and the tow behaviour has been analysed using orthotropic finite elements. By proceeding in this way the orthotropic description of tow behaviour is traceable to both fibre and matrix properties, with all the physics of their interactions being taken into account; and, in this way the approach links the micro response of the individual composite constituents with the macro responses of the RVEs and the structural components that they are used to model. In this way the multi-axial stress–strain response, and the damage/degradation of material properties, of the 8-Harness satin weave composite have been analysed.

An idealised unit cell of the composite is shown schematically in Fig. 1. The HITCO C/C 8-Harness satin weave is comprised of T300 carbon fibre tows woven together to form a satin cloth or lamina. Nine such laminae are stacked and the material is then infiltrated to form a sheet of the composite. Further details of the material and its manufacturing route are provided by Tang et al. (2011a). Sheikh et al. (2009) have reported uni-axial test data on the material for variation of stress and through-thickness thermal conductivity with axial strain, which will be used here to judge the fidelity of the analytical approach. The next section introduces the mechanical behaviour of a HITCO composite tow.

2. Mechanical behaviour of a uni-directional CMC tow

This section addresses typical mechanical behaviour of a uni-directional tow subjected to different loading conditions; and the influence of the different damage modes on the stress–strain response.

2.1. Longitudinal stress–strain response

Under uniform straining in the fibre 3-direction, as shown in Fig. 2a, a uni-directional fibre-reinforced ceramic matrix tow exhibits the typical longitudinal stress–strain response shown in Fig. 2b (c.f. Hayhurst et al., 1991). The characteristic stages of the stress–strain response are described below (Tang et al., 2009):

- **AB**: initially, the composite behaves as an undamaged, linear elastic material.
- **BC**: matrix cracking takes place (Fig. 2c).
- **CD**: fibre–matrix interface failure and wake debonding occurs as shown in Fig. 2d, and the weaker fibres fail as shown in Fig. 2e.
- **DE**: the majority of fibres fail and pull-out against a frictional stress takes place along the wake debonded interface, as illustrated in Fig. 2f.

The term "wake debonding" used in Fig. 2d refers to failure of the fiber–matrix interface that leaves rough, partly fractured

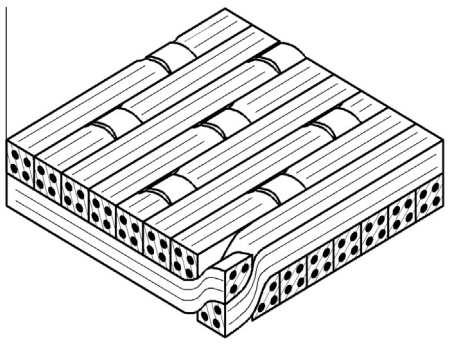

Fig. 1. Schematic of the unit cell of the 8-Harness satin weave HITCO material.

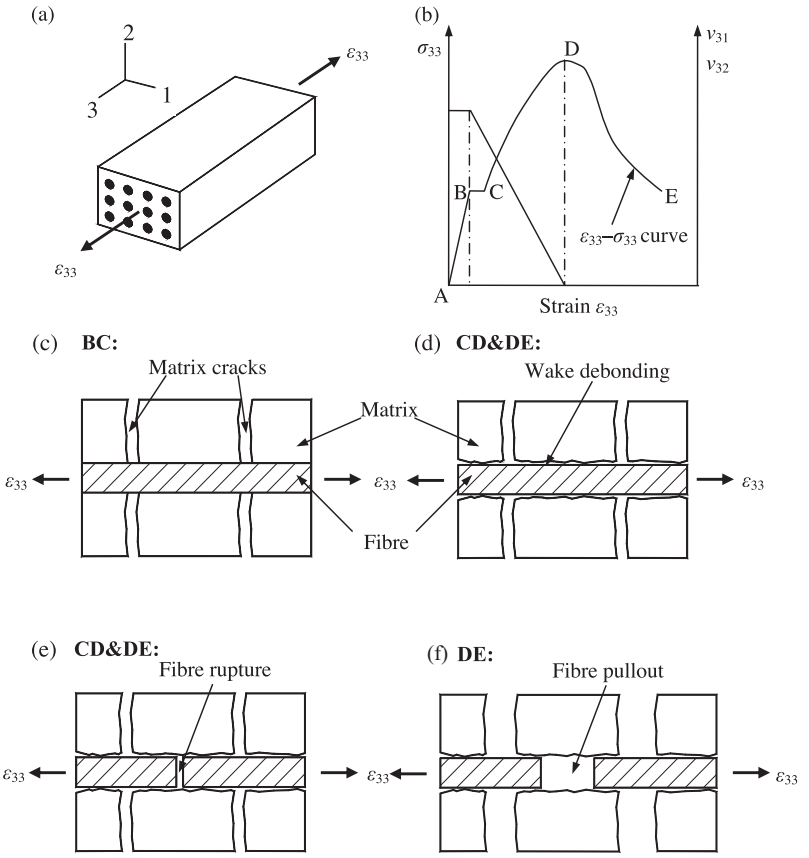

Fig. 2. Schematic drawings of: (a) a uni-directional tow under longitudinal extension; (b) longitudinal stress–strain and Poisson's ratio-strain curves; and (c)–(f) corresponding damage modes.

interfaces that rub against each other, generating frictional forces as they experience relative sliding.

2.2. Variation of Poisson's ratio with strain

The idealised variation of Poisson's ratio with longitudinal strain is shown in Fig. 2b. The justification for this simplification is given by the experimental data of Karandikar and Chou (1993) shown in Fig. 3 for a uni-directional Nicalon/CAS composite. They used a uni-axial specimen of 150 mm in length and 12.5 mm in width, with the strains reported in Fig. 3 being measured by strain gauges with 5 mm gauge length; and, the saturation spacing of the matrix cracks was of the order of 125 μm. The tri-linear idealisation is given by the broken line ABD, where the letters refer to Fig. 2b. The latter data has also been corroborated by finite element studies done using representative volume elements of CMCs by Tang et al. (2011b). From Fig. 2b it can be seen that initially, Poisson's ratio remains constant until point B, where matrix cracking occurs, it then decreases linearly due to wake debonding, and finally approaches zero at the peak stress D. The effect of transverse cracking and local delamination on Poisson ratio has been extensively discussed for laminated composites by Lubineau (2010), Bordeu et al. (2010) and Ladeveze and Lubineau (2003); and, extension of the approach to CMC is straightforward.

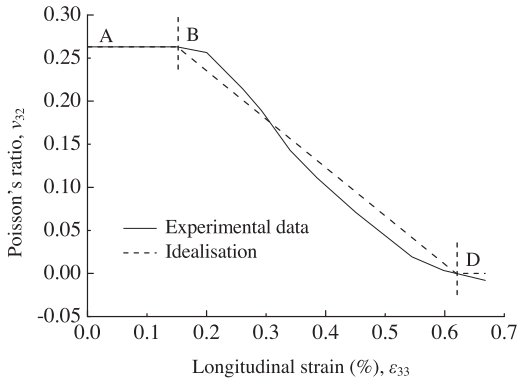

Fig. 3. Measured (Karandikar and Chou, 1993) and idealised variation of Poisson's ratios with longitudinal strain. Letters A, B and D refer to Fig. 2b.

2.3. Tow deformation and failure for transverse tension

A uni-directional tow subjected to transverse tension, as shown in Fig. 2a, is assumed to deform in a linear elastic manner. The transverse Young's modulus and the Poisson's ratio, v_{21} are defined in Fig. 4b and c respectively; they are assumed to be constant until the occurrence of fibre–matrix debonding and/or matrix cracking, shown in Fig. 4d. At that instant the damaged is assumed to be instantaneous and results in a complete loss of strength. Consequently, after fibre/matrix debonding and/or matrix cracking, the model assumes the stress to immediately fall to zero.

2.4. Tow deformation and failure for transverse shear

The shear stress–strain response for the tow (Blacklock and Hayhurst, 2011) shown in Fig. 5a is given in Fig. 5b; it is assumed to have the same characteristics as the transverse behaviour of Fig. 4b. On loading, the shear stress increases linearly with the

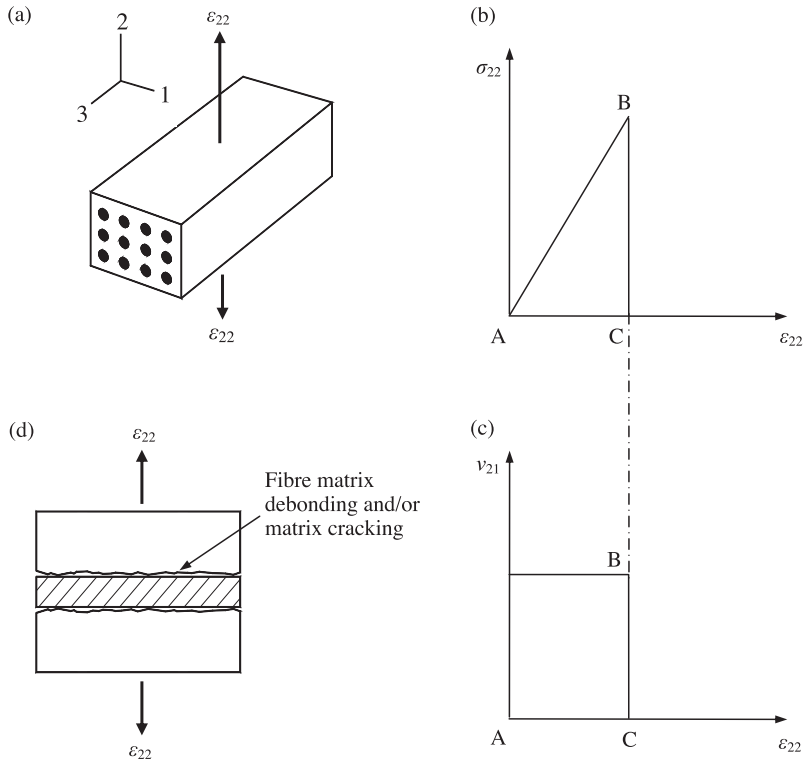

Fig. 4. Schematic drawings of: (a) a uni-directional tow under transverse straining; (b) and (c) transverse stress–strain and Poisson's ratio curves; and (d) schematic of corresponding damage modes.

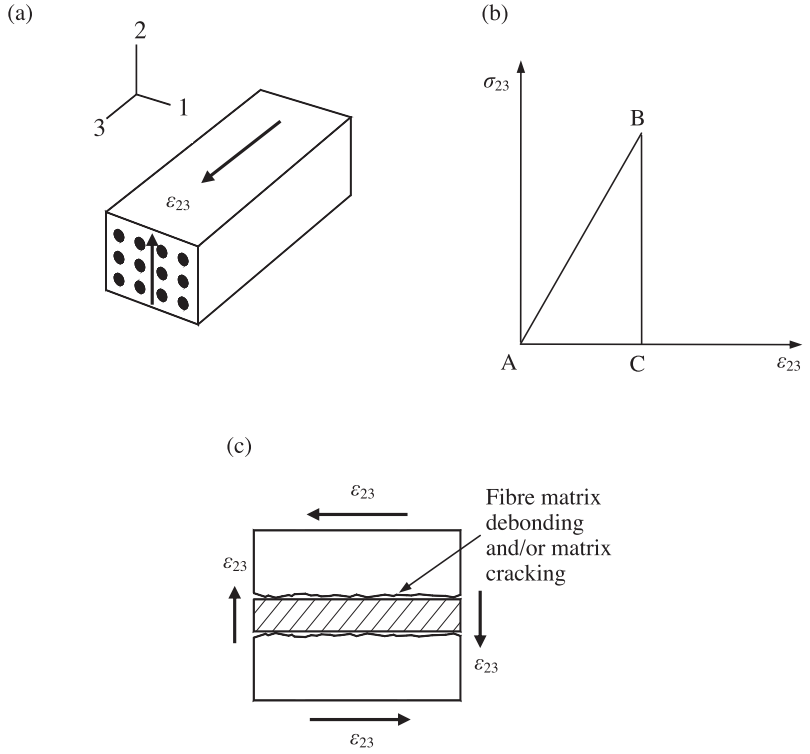

Fig. 5. Schematic drawings of: (a) a uni-directional tow under shear straining; (b) shear stress–strain curve; and (c) corresponding damage modes.

shear strain, as shown in Fig. 5b until a critical value is reached, at which point the model assumes catastrophic shear failure takes place as shown in Fig. 5c, and the shear stress immediately drops to zero.

2.5. Alternative stress–strain models for transverse tension and shear

In a later section the models defined in Figs. 4 and 5 for catastrophic tow failure, which have been employed successfully by

Zhang and Hayhurst (2010) for the carbon fibre, carbon/SiC matrix composite DLR-XT that cracks on a scale of the order of the tow width, are found to be too extreme. And alternative models for the HITCO material will be examined that permit a more gentle strain dependent degradation of the transverse and shear moduli; they avoid failure of the amorphous carbon matrix, and instead allow moduli degradation to take place through continuum damage micro-cracking on the scale of the fibre radius. This will result in a non-catastrophic loss of stiffness. These models will be defined in detail in a later section, and the results of analyses on a partial unit cell of the composite will then be presented.

2.6. Longitudinal stress–strain response under multi-axial loading

When a uni-directional tow is simultaneously subjected to two or more independent loading systems, e.g. longitudinal, transverse, and shear loading, mechanistic interactions can take place. The effects of transverse tension or shear stress on the longitudinal stress–strain response are reflected in experiments done on a range of CMCs that have been reported by Sheikh et al. (2009); these are now addressed.

For a uni-directional tow under longitudinal uni-axial loading, the material exhibits ductile behaviour, which is demonstrated as the gentle decreasing stress–strain curve after the peak in Figs. 2b and 6a (Blacklock and Hayhurst, 2011). This is due to wake debonding of the fibre–matrix interface that occurs gradually, and creates a partially intact fibre–matrix interface, which allows a failed fibre to pull out against a frictional stress along the wake debonding interface, c.f. Fig. 2f. This occurs within individual blocks, where a block is defined by a single fibre and its associated matrix that is contained between two adjacent matrix cracks. This phenomenon has been discussed in detail by Tang et al. (2009). The variation within a tow of the normalised number of wake debonded blocks, N/N_T, where N_T is the total number of blocks in a tow, with composite strain, $(\varepsilon_{33})_\infty$, is shown in Fig. 6a. When a uni-directional tow is subjected to multi-axial loading, a positive transverse stress or a shear stress advances wake debonding, and also degrades the partially intact interface to a non-contacting interface. Hence the frictional stress reduces to almost zero and the pullout mechanism is weakened.

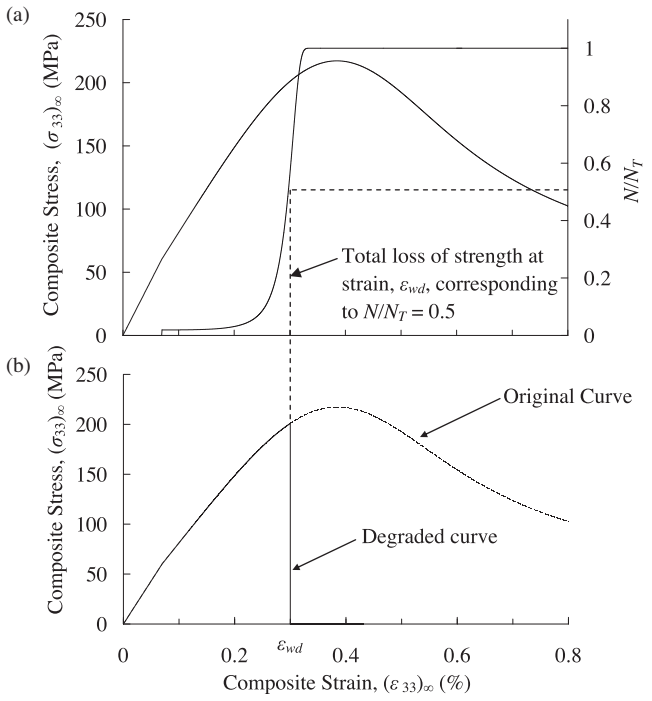

Fig. 6. Material properties for a C/C composite: (a) stress–strain curve of a uni-directional tow under longitudinal loading and variation of normalised number of wake debonded blocks N/N_T with composite strain $(\varepsilon_{33})_\infty$; and (b) stress–strain curve of a uni-directional tow under multi-axial loading (Blacklock and Hayhurst, 2011).

Even though the strength of the pull-out mechanism is reduced, it cannot explain the catastrophic fibre failure observed in the experiments reported by Sheikh et al. (2009). A further mechanism, known as ***dynamic fibre failure by instantaneous pullout deactivation*** (Blacklock and Hayhurst, 2011), is believed to be the cause of brittle failure. In this mechanism it is postulated that one half of all blocks in a tow ($N/N_T = 0.5$, at the strain ε_{wd} shown in Fig. 6a) simultaneously undergo instantaneous wake debonding and fibre pull-out deactivation. Ductile CMCs are designed so that the average wake debonding strain, ε_{wd}, is slightly less than the peak composite strain; and hence, at this point, the fibres are stressed to a high fraction of the average fibre failure stress. When further degradation and failure of the fibre–matrix interfaces take place, shear stress waves are released c.f. Fig. 2d; waves propagate away from both matrix cracks at the extremities of the block; and to maintain equilibrium a tension stress wave is induced in the fibre. The tension wave moves at a higher velocity than the shear wave, and the two fibre tension waves meet at the centre of the block, and reflect as a fibre tension wave with twice the amplitude of the incident wave. The doubling of the tensile stresses in the fibres causes local failure of the fibre. This local mechanism can occur simultaneously: at several points along the same fibre; in several fibres in the same tow; and, in different tows. Interactions between the events at different locations take place through the need to satisfy global equilibrium and strain compatibility. Axial stress redistributes to adjacent fibres causing more widespread failure of fibres and tow. By this mechanism, the original curve (Fig. 6b), which corresponds to a uni-directional tow under longitudinal loading only, switches to the degraded curve, which is for a tow subjected to multi-axial loading.

In the next section, the finite element formulation of the 8-Harness satin weave HITCO problem will be addressed.

3. Formulation of the finite element model

A uni-directional tow or lamina has been chosen as the basic constituent in the finite element model, and therefore a portion of a tow or a lamina that consists of thousands of fibres embedded in the matrix can be represented by a single 8-node solid finite element as shown in Fig. 7. The material properties were assumed to be multi-linear elastic and the stress–strain and the Poisson's ratios-strain curves shown in Figs. 2, 4 and 5 were used in the constitutive equations. The finite element package ABAQUS (SIMULIA, 2008), with a user-defined subroutine UMAT, was used to perform the analysis. In this way the approach models a portion of a tow using a single finite element with orthotropic properties; and has the advantage of simplicity in comparison to the binary system of modelling (Xu et al., 1995). This is a consequence of having only one component; and, unlike the binary method which has two components (i.e. fibres and matrix or medium), does not have the difficulties associated with calibration of medium properties.

3.1. Homogenisation of a uni-directional tow

A heterogeneous uni-directional tow or lamina has been homogenised to a single block as shown in Fig. 7. The block has the same overall dimensions and equivalent orthotropic material properties as the HITCO tow. There are nine independent material properties:

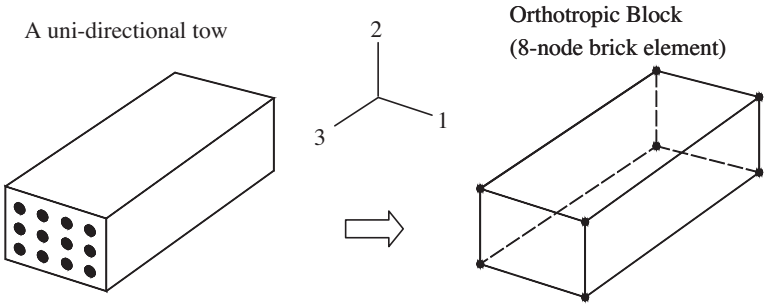

Fig. 7. Homogenisation of a uni-directional tow or a uni-directional lamina to a single orthotropic block.

Young's moduli: E_3, E_2, and E_1.
Poisson's ratios: v_{31}, v_{32}, and v_{12}.
Shear moduli: G_{12}, G_{23}, and G_{13}.

The use of nine independent materials parameters in this homogenisation procedure is necessary to model the highly orthotropic behaviour of the CMC tow (Yang and Cox, 2003).

3.2. Discretisation of the stress–strain curve and definition of the constitutive equations

The analysis of the composite behaviour was carried out on a partial unit cell composed of four tows, each having several homogenised orthotropic finite elements. To perform the finite element analysis, the non-linear longitudinal stress–strain relationship was discretised to a multi-linear curve. The loading was applied to the unit cell in terms of displacement boundary conditions, i.e. displacement rather than load controlled conditions were imposed. The applied displacement was divided into many small increments. For each increment, the constitutive equation used for the orthotropic material was:

$$\{\Delta\boldsymbol{\sigma}\} = [\mathbf{C}(\Delta\boldsymbol{\varepsilon})]\{\Delta\boldsymbol{\varepsilon}\}, \tag{1}$$

where $\{\Delta\boldsymbol{\sigma}\}$ is the stress increment vector, $[\mathbf{C}(\Delta\boldsymbol{\varepsilon})]$ is the incremental stiffness matrix, and $\{\Delta\boldsymbol{\varepsilon}\}$ is the strain increment vector. The derivation and explicit form of the equation is given in Zhang and Hayhurst (2010), and for convenience is repeated in Appendix A.

The strain driven formulation has been selected since to best deal with local unloading difficulties. In this way all the problems associated with a load-based formulation have been avoided. The approach has been to maintain a level of simplicity that is commensurate with the quality of data available for the materials under study.

3.3. Activation of dynamic tow failure on fibre fracture by instantaneous pullout deactivation

To model the activation of the dynamic fibre failure mechanism, by instantaneous pullout deactivation, under multi-axial loading, introduced in Section 2.5, two assumptions are made: (a) the switch from the original stress–strain curve to the degraded curve is activated by a small finite positive transverse stress, or by a small non-zero shear stress; and (b) as a consequence, the decrease of the Poisson's ratios, v_{31} and v_{32} commences at the matrix cracking strain ε_{wd}, as shown in Fig. 6a, and were taken to zero at the wake debonding strain, as opposed to the strain at peak load, D, given on the curve of Fig. 2b for the uni-axially strained tow. The assumptions made are based on the effects of instantaneous fibre pullout deactivation as discussed in Section 2.5.

3.4. Implementation of the UMAT in ABAQUS

The finite element analysis was carried out using the package, ABAQUS/standard and a user defined subroutine, UMAT, to perform the calculations associated with the multi-linear constitutive equations. The multi-axial elastic properties, the constitutive equations, and the activation of the dynamic composite failure on fibre fracture by instantaneous pullout deactivation were defined in the UMAT. During each increment, the UMAT read the strains at each material point, and then assigned the corresponding Young's moduli, Poisson's ratios and shear moduli. The constitutive equations were then used to calculate the stress fields. Nine solution-dependent state variables, STATEV, were used to record different damage modes and to control their interactions. The initial values of STATEV, were set to 0; and when the damage state changes, i.e. transverse cracking, shear failure, or dynamic fibre failure occurs, the values of STATEV were set to be 1. The STATEV values associated with the Poisson's ratios, v_{31} and v_{32}, are controlled by the dynamic fibre failure. Once STATEV values are equal to 1, the material properties take very small finite values, no matter what the local strains are.

Automatic incrementation algorithms and the increment redefinition variable, PNEWDT, were continuously updated to ensure that the discretised points were located exactly at the end of the relevant increments.

In the UMAT, the material Jacobian matrix has to be provided for the mechanical constitutive model. Incorrect definition of the material Jacobian usually influences only the convergence rate; and, the results (if achieved) are unaffected (SIMULIA, 2008). However, an inaccurate Jacobian matrix may cause computational failure due to solution divergence. If rapid convergence of the analysis is to be achieved then the Jacobian matrix must be accurately determined. The approach for the evaluation of the material Jacobian matrix is given in Appendix A for the constitutive equation (1).

3.5. Load path algorithm

Post-peak behaviour of composites and the associated loss of uniqueness, can pose a problem. This leads to zones of composite unloading with adjacent zones loading, whilst both zones are subjected to increasing strain, hence compatibility can be satisfied whilst equilibrium may be violated. To model the influence of fibre fracture by instantaneous pull-out deactivation on dynamic tow failure, load paths were introduced into the finite element method. A load path consists of a series of elements which form a continuous tow or lamina, e.g. elements in a longitudinal tow or elements in an orthogonal tow. The introduction of the load path algorithm is to model the damage mechanism of dynamic tow failure in a homogeneous aspect, but not to evaluate the failure mechanism locally. Although the load path is prescribed as a prerequisite and this choice is mathematically arbitrary, the load path of a continuous tow is consistent with the physical representation of the HITCO

material, where its mechanical behaviour is dominated by the longitudinal properties of woven tows. It was assumed that:

(1) When the local longitudinal strain of an integration point (master point) in a load path, reaches 90% of the wake debonding strain, ε_{wd}, then the Poisson's ratios, v_{31} and v_{32}, of all the other integration points (slave points) in the load path decrease proportionally with the reduction in the corresponding variable at the master point. The Poisson's ratios, v_{31} and v_{32}, of all the integration points reduce to zero when the longitudinal strain of the master point reaches the wake debonding strain, ε_{wd}.
(2) Following that, elements in all load paths were allowed to fail simultaneously, and all stress components were unloaded to zero. The unloading slope was selected to be as steep as possible, compatible with the maintenance of numerical stability. This algorithm was implemented in the UMAT by reading element numbers in each load path that were stored in a data file. To facilitate the unloading computation, a scaling factor, determined by the fractional reduction of the stiffness at the master point was used to evaluate the degraded stiffness at the slave points. The unloading of a load path is implemented in an implicit way; with the calculation performed as in a static analysis without loading rate dependence.

3.6. Implementation of the incremental constitutive law

For each increment in the finite element analysis, the incremental constitutive law, Eq. (A.9), has been implemented using the following steps:

(1) Determine the nine material properties from the local strains and multi-linear curves.
(2) Identify the damage state and update the state variable, STATEV. If the dynamic fibre failure criterion is satisfied, then the load path algorithm is activated.
(3) Update the stress increments using the incremental constitutive equation (A.9).
(4) Update the material Jacobian matrix using Eq. (A.11).

4. Definition of partial unit cell for HITCO 8-Harness satin weave

A plan view of the entire unit cell is shown schematically in Fig. 8a, this view replicates the isometric view of Fig. 1. To reduce the number of finite elements used to model the HITCO 8-Harness satin weave, and also to alleviate numerical difficulties that can arise with modelling localised unloading within the repeated woven zones, eight in total for the 8-Harness satin weave, of the entire unit cell, a minimal repeatable sub-unit has been sought. The minimal or partial unit cell/sub-unit selected is that associated with the square region of the weave that is defined by the outer broken line in Fig. 8a and b. For purposes of finite element analysis this can be reduced further to the quadrant, shown in Fig. 8c. In this figure the points X_{1a} and X_{3a} are on the centre lines of orthogonal tows. The dimensions defined in Fig. 8b and c have been determined on a volumetric basis, such that the volume of the partial unit cell square in Fig. 8b, of unit thickness, is $(2X_{2b})(2X_{3b})$, which in turn is one eighth of the volume of the entire unit cell of Fig. 8a, i.e. $(4a\ 4a)/8$. Given that $X_{2b} = X_{3b}$, it can then be shown that $2X_{2b} = 2X_{3b} = \sqrt{2}a$. The finite element analysis has been carried out on the partial unit cell of Fig. 8c using periodic boundary conditions.

5. Formulation of the finite element partial unit cell model

Fig. 9a shows two 0° tows, dark shading, and two 90° tows, light shading, and Fig. 9b shows the assembled tows that make up the entire partial unit cell. An important objective of this study is to develop an approach which is capable of analysing large scale composites and engineering components. This makes it a very difficult task to create a finite element model, which captures woven features of a tow yet uses a minimum number of finite elements. The mesh and geometry of the HITCO 8-Harness satin weave partial cell shown in Fig. 9 is believed to be a near optimal solution. The mesh for a single woven tow consists of 16 elements: three 8-node brick elements, nine 6-node wedge elements, and four 4-node tetrahedral elements; and the mesh for a single straight tow consists of 20 elements: seven 8-node brick elements, nine 6-node wedge elements, and four 4-node tetrahedral elements. The HITCO 8-Harness satin weave partial unit cell model is an assembly of four tows c.f. Fig. 9b, which are bonded together through the fully contacted interfaces. Inevitably, the small number of elements will incur some loss of accuracy. However, it is these features that make possible the finite element analysis of large components. Yang and Cox (2003, 2010) concluded that strains averaged over a gauge volume whose linear dimensions are equal to or exceed half the cross-sectional dimensions of a tow, are reasonably mesh independent. For the present HITCO 8-Harness satin weave partial unit cell model, the majority of the elements (93.3% by volume) are approximately equal to this gauge volume; and, in addition their strain distributions are rather uniform. Hence, it is reasonable to use the local strain at an integration point to predict different failure modes of the material. The fidelity of the model will be assessed by using the stress–strain experimental results of Sheikh et al. (2009).

The geometry of a single woven tow, shown as the lower illustration in Fig. 9a, is given in Fig. 10. By reference to Fig. 9a, and by virtue of symmetry, the dimension of the non-woven tows may be deduced.

6. Modelling of tow waviness

During manufacture of the HITCO 8-Harness satin weave composites, some degree of waviness in the alignment of the fibres or tows is introduced. The weave angle and the degree of waviness have been obtained from the micrographs presented by Sheikh et al. (2009). To the knowledge of the authors, this is the only information available in the literature, and measurements have been taken from that source. The value of the weave angle is $\zeta = 9.4°$; and the average waviness angle is $\xi = \pm 2.44°$. The latter value has been used in the finite element model to evaluate the effects of waviness on stiffness reduction. Both the in-plane and out-of-plane waviness is modelled in the finite element analysis by assigning an associated local material orientation to each individual element. Fig. 10 shows the fibre directions and their waviness angle of $\xi = \pm 2.44°$. To assess the effects of waviness on composite behaviour, stress–strain curves have additionally been predicted for zero waviness angle $\xi = 0°$. A periodic boundary condition was applied to the partial unit cell to simulate uni-axial straining along the 0° fibre direction (the 3 direction in Fig. 9).

7. HITCO C/C tow material properties

Blacklock and Hayhurst (2011, 2012) reported the initial elastic properties and multi-axial failure behaviour of HITCO fibre tows. The initial elastic properties were predicted based on a micro-mechanical finite element analysis of representative volume elements from the constituent properties of fibres and matrices.

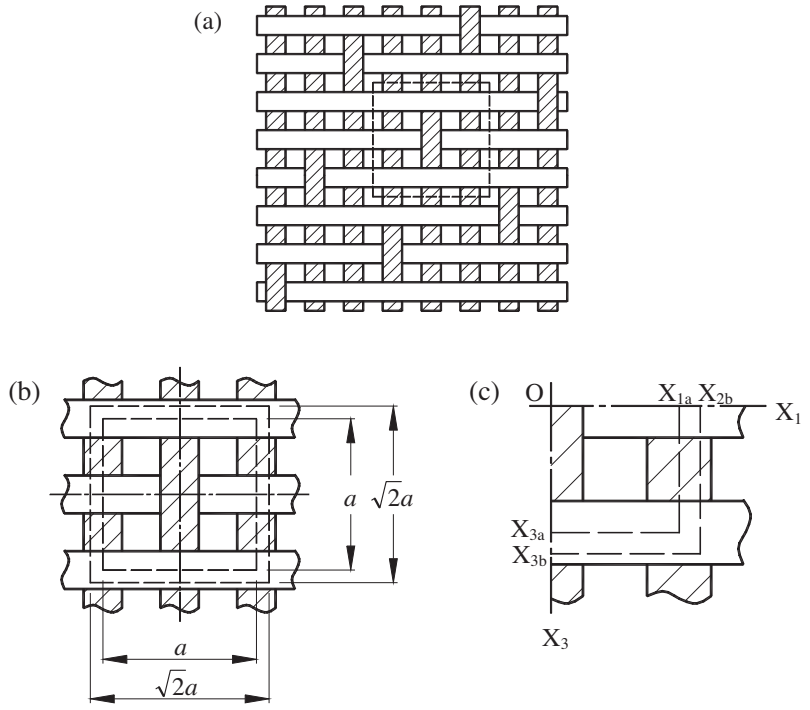

Fig. 8. Definition of partial unit cell. (a) Plan view of entire unit cell shown schematically in Fig. 1. (b) Weave segment identified in (a) by broken line square boundary. (c) Definition of a single quadrant of the partial unit cell shown in (b).

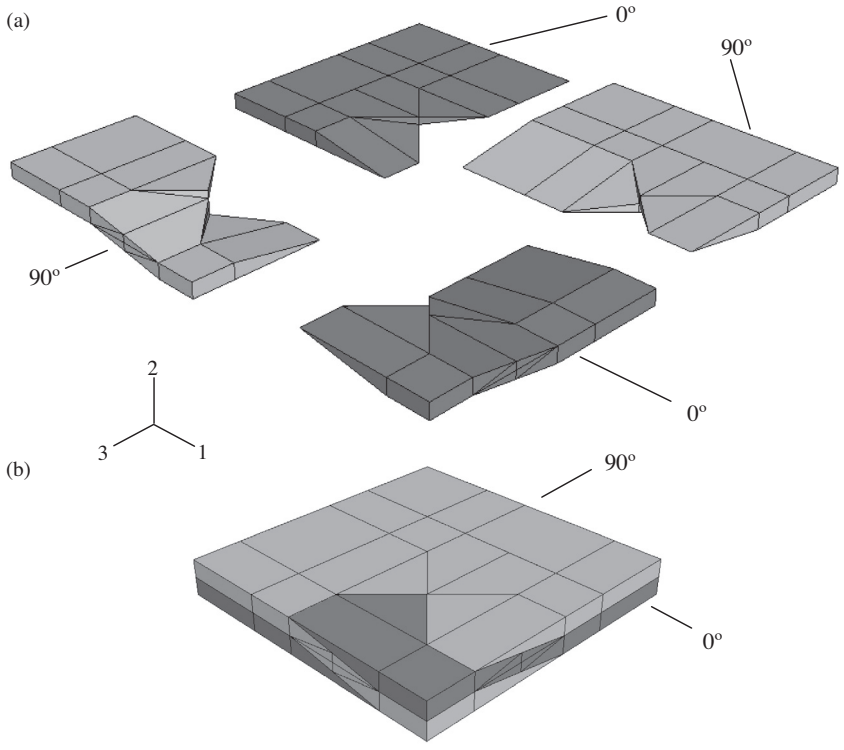

Fig. 9. Finite element mesh of a single quadrant of the partial unit cell shown in Fig. 8c: (a) exploded view showing 0° tows, dark shading, and 90° tows, light shading. (b) Assemblage of tows, shown in (a), to form one quarter of the partial unit cell.

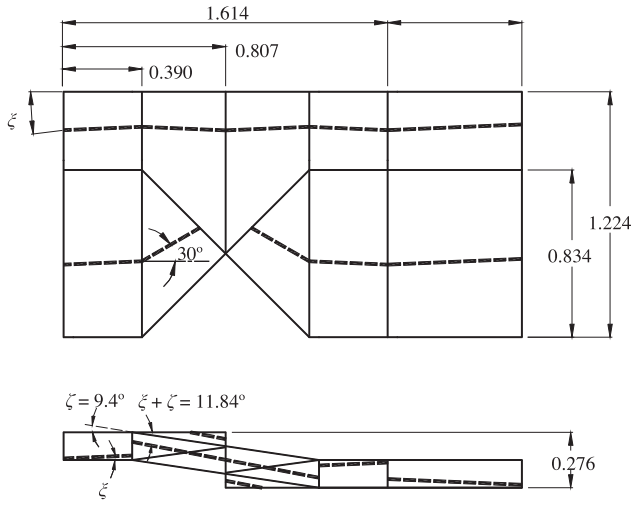

Fig. 10. Geometry of a single woven tow, shown as the lower illustration in Fig. 9a. Tow waviness is shown by the broken thick line, and defined by the waviness angle $\xi = \pm 2.44°$. The weave angle is $\zeta = 9.4°$. All linear dimensions are given in mm.

The longitudinal stress–strain curve of the uni-directional HITCO fibre tows under multi-axial loading were obtained using the physical model of Hayhurst et al. (1991) and Tang et al. (2009); and the fracture behaviour was modelled by the mechanism proposed by Blacklock and Hayhurst (2011) involving dynamic fibre failure by instantaneous pullout deactivation. Elastic properties used in the finite element model are given in Fig. 11. The discretised longitudinal stress–strain curves are shown in Fig. 11a, where the solid line is the original curve, which is for a uni-direction tow under longitudinal straining only, and the broken line is the degraded curve, which takes account of dynamic fibre failure at $\varepsilon_{33} = \varepsilon_{wd}$. The variation of Poisson's ratios, v_{12}, v_{31} and v_{32}, with longitudinal strain are shown in Fig. 11b.

With regard to the deformation and failure behaviour of tows under transverse tension and shear, two models will be studied. These are now addressed

7.1. Transverse brittle tow failure

The stress–strain curves corresponding to this mechanism are shown in Fig. 11c and d. In physical terms the loss of strength corresponds to the formation of cracks transverse to the tow. The initiation of the cracks is either associated with the matrix or the fibre–matrix interface, and growth takes place to generate a continuous crack or set of cracks across the tow section, whose length is expected to be of the order of the tow width. The transverse stress–strain, shear stress–stain curves of Fig. 11c and d respectively are shown with bi-linear broken lines as in Figs. 4b and 5b; however, it was not possible to achieve numerical convergence for the discontinuous nature of this representation, and both curves had been smoothed around the peak of the reference curves as shown in Fig. 11c and d, but the fracture energy covered by the reference curves and the corresponding smoothed curves are identical.

This is the model utilised by Zhang and Hayhurst (2010) for the carbon fibre, SiC/carbon matrix composite DLR-XT; and for that materials system, the transverse cracks would be expected to occur in the SiC component of the matrix. However, for the C/C HITCO material studied here this is not expected to be the case due to the amorphous nature of the carbon, and in addition an alternative proposal will also be considered.

7.2. Transverse tow failure by strain controlled moduli degradation

In the C/C HITCO material only one amorphous carbon matrix exists. Unfortunately, no micrographic evidence is available to guide the formulation of a relevant model, and an inverse approach will be adopted: a model will be postulated, its effects predicted at the partial unit cell level, and its efficacy assessed. It is thought that

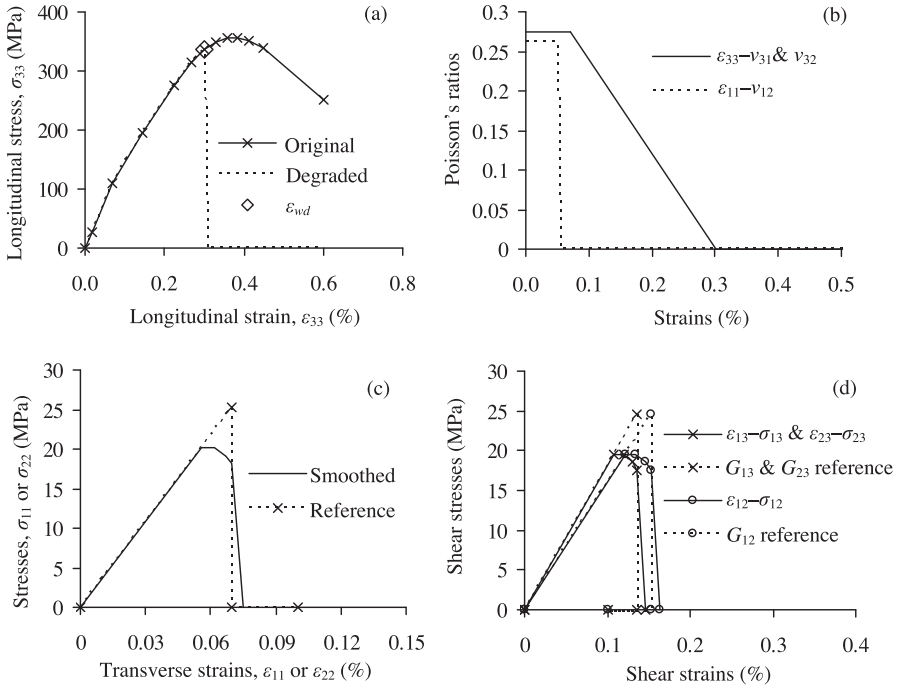

Fig. 11. Material properties of HITCO C/C tow: (a) longitudinal stress–strain curve (b) through-thickness stress–strain curve (c) longitudinal transverse Poisson's ratios, v_{31} and v_{32} and (d) longitudinal through-thickness shear stress–strain curve.

a continuum of micro-cracks may form at the scale of the fibre radius, and result in a very gentle degradation of moduli that is controlled by the strain dependence of the associated transverse modulus. The model has been formulated as follows.

The transverse moduli E_{11} and E_{22}, and the shear moduli G_{12}, G_{13} and G_{23} degrade in sympathy with the corresponding direct modulus E_{ii} (ε_{ij}) such that:

$$E_1 = E_2 = E_1(\varepsilon_{11}=0)\left\{\frac{E_3(\varepsilon_{11})}{E_3(\varepsilon_{11}=0)}\right\}, \text{ and}$$
$$G_{12} = G_{12}(\varepsilon_{12}=0)\left\{\frac{E_1(\varepsilon_{12})}{E_1(\varepsilon_{12}=0)}\right\};\quad G_{13} = G_{13}(\varepsilon_{13}=0)\left\{\frac{E_1(\varepsilon_{13})}{E_1(\varepsilon_{13}=0)}\right\};$$
$$G_{23} = G_{23}(\varepsilon_{23}=0)\left\{\frac{E_2(\varepsilon_{23})}{E_2(\varepsilon_{23}=0)}\right\}. \tag{2}$$

The Poisson's ratios have been evaluated as follows:

$$\text{for}\quad \varepsilon_{11} \leqslant 0.07\%,\quad \nu_{12} = 0.262,\quad \text{and}$$
$$\text{for}\quad 0.07 \leqslant \varepsilon_{11} \leqslant \hat{\varepsilon},\quad \nu_{12} = 0.262 - \left\{\frac{0.262}{\hat{\varepsilon} - 0.07\%}\right\}\varepsilon_{11}, \tag{3}$$

where $\hat{\varepsilon} = \varepsilon_{wd} = 0.3\%$ strain for catastrophic failure, and $\hat{\varepsilon} = 0.38\%$ is the peak tow strain. This approach is consonant with the experimental evidence discussed in relation to Fig. 3 for values of the Poisson's ratios, and the model will be referred to as transverse tow failure by strain controlled moduli degradation.

In the next section the results of analyses are presented for the partial unit-cell.

8. Stress–strain predictions of the partial unit cell for HITCO 8-Harness satin weave

8.1. Models for tow failure

Several finite element predictions have been made for different conditions and assumptions, these include: values of fibre/tow waviness of $\xi = 0°$ and $\xi = \pm 2.44°$; the two transverse failure models, transverse matrix fracture (Fig. 11c), with transverse moduli degradation equations (2) and (3); and, tow failure either by dynamic fibre failure by instantaneous pullout deactivation, or by deformation limited failure; the latter will be elaborated in a later section. These failure criteria have been implemented in the finite element UMAT by identification of the element integration point which has the largest local axial component of strain ε^{ℓ}_{33}. The selection of this node has been assisted by the use of axial strain field plots of the type shown in Fig. 12, where the results are presented for: waviness $\xi = \pm 2.44°$, transverse brittle tow failure, and dynamic composite failure on fibre fracture by instantaneous pullout deactivation. The most highly strained node, presented in the strain field plot, ε^{ℓ}_{33}, of Fig. 12, is located in the straight tow in an element that is adjacent to the weave zone of the adjoining tow. This point becomes the master point at which the local strain is used to control unloading in the load paths as described in Section 3.4 (i). Two partial unit cell failure modes have been identified. Firstly, dynamic composite failure on fibre fracture by instantaneous pullout deactivation when the local strain at the control node $\varepsilon^{\ell}_{33} = \varepsilon_{wd} = 0.3\%$. And secondly, composite failure by deformation localisation is allowed when the local strain ε^{ℓ}_{33} is permitted to increase, overriding other failure mechanisms, until deformation is localised in the coloured band of Fig. 12, adjacent to the weave zone. At this point the stress σ^{ℓ}_{33} across the band begins to decrease, axial equilibrium can no longer be satisfied and failure ensues.

These aspects are each addressed in turn in the following section, after the experimental stress–strain data for the HITCO composite has been introduced.

8.2. Experimental stress–strain curves for the HITCO composite

The results of experiments carried out on uni-axial testpieces manufactured from the HITCO 8-Harness satin weave material have been reported by Sheikh et al. (2009). Four tests were performed and the stress–strain curves for three tests have been reproduced in Fig. 13. One test result, which is essentially the same as that for Exp 4, has been omitted. This is due to the associated thermal data, not considered here, being erroneous. Two classes of behaviour were observed: two tests exhibited brittle behaviour, c.f. Exp 4 of Fig. 13, without evidence of controlled unloading, and two tests showed a "flat topped stress–strain curve" followed by stable unloading, i.e. quasi-ductile behaviour, c.f. Exp 1 and 2 of Fig. 13.

8.3. Predictions made using composite failure by deformation localisation

8.3.1. Composite stress–strain response for the matrix transverse brittle tow failure (Fig. 11c)

Predictions have been made for the matrix fracture model, defined in Fig. 11c, with waviness angle $\xi = 0°$, and for composite failure by deformation localisation. The prediction of Fig. 13 shows that the composite stiffness is grossly under-estimated for strains in excess of 0.06%. However, the failure strain obtained for composite failure by deformation localisation is in good agreement with the results of Exp 1 and Exp 2; and does not agree with the test result for Exp 4. This indicates that the constitutive model used for the transverse straining of the tow is incorrect. Several possible solutions have been sought. The first is to increase the tow axial

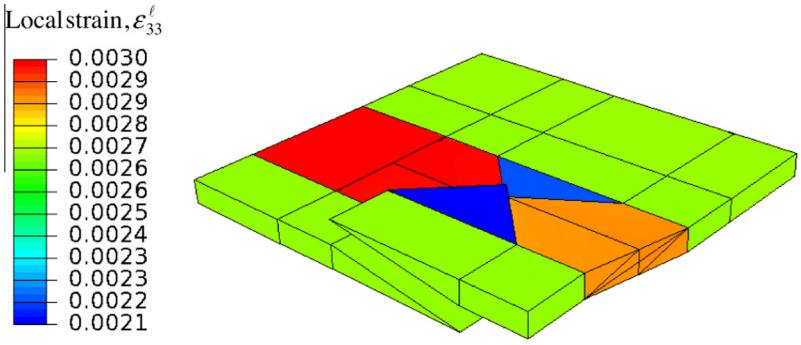

Fig. 12. Field plot of tow strain ε^{ℓ}_{33}, defined in local coordinates, over two adjacent 0° tows; 90° tows are not shown for clarity. See Fig. 9a in which the 0° tows are shown separately in dark shading, and Fig. 9b for local coordinates. Levels of strain are given prior to failure by deformation localisation. The zone of strain localisation is confined to a band passing through the woven section of the tows.

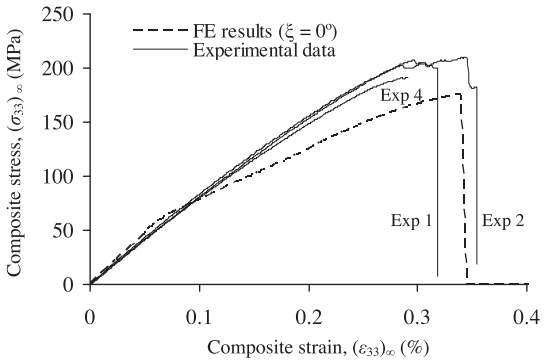

Fig. 13. Comparison of experimental stress–strain curves for the HITCO 8-Harness satin weave C/C laminate with the curve predicted for $\xi = 0°$ waviness, the transverse brittle tow failure stress–strain curve, given in Fig. 11c, and composite failure by deformation localisation.

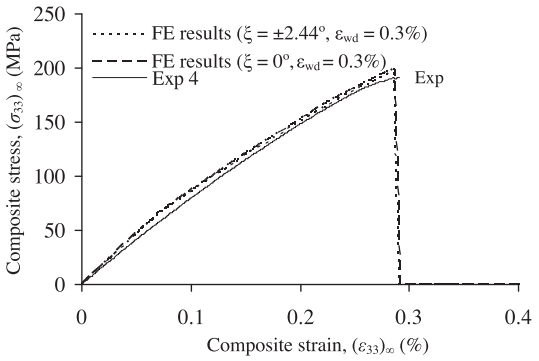

Fig. 15. Comparison of an experimental stress–strain curve for the HITCO 8-Harness satin weave C/C laminate with curves predicted for $\xi = 0°$ and $\xi = \pm 2.44°$ levels of waviness and the transverse tow stress–strain curve given by the coupled damage stiffness reduction model. Failure has been modelled by dynamic fibre failure by instantaneous pull-out deactivation.

stress–strain curve predicted by the model of Tang et al. (2009). This proved not to be possible, since the average fibre failure stress and the associated Weibull index were accurately assigned and the variations to the extremes of tolerance/accuracy would not achieve the necessary increases in strength. Guidance was sought from the work of Tang and Hayhurst (2011) in which the transverse modulus was set to a value that neglected transverse matrix cracking, and was based on the initial transverse moduli determined by Blacklock and Hayhurst (2012). Hence the similar approach described by Eqs. (2) and (3) has been adopted here.

8.3.2. Composite stress–strain response for transverse tow failure by strain controlled moduli degradation equations (2) and (3)

The calculations reported in the previous section have been repeated for exactly the same conditions, but with the inclusion of transverse tow failure by strain controlled moduli degradation described by Eqs. (2) and (3), and the results are presented in Fig. 14. In addition, results are also presented for waviness values of $\xi = \pm 2.44°$. For both waviness values of $\xi = 0°$ and $\xi = \pm 2.44°$ the predictions are in close accord with data for the test results of Exp 1 and Exp 2, and the prediction for the waviness angle of $\xi = \pm 2.44°$ is in good agreement with the larger failure strain of Exp 2.

8.4. Predictions made for dynamic composite failure with fibre fracture by instantaneous pullout deactivation

Finite element predictions have been made for two levels of waviness $\xi = 0°$ and $\xi = \pm 2.44°$ and for dynamic composite failure

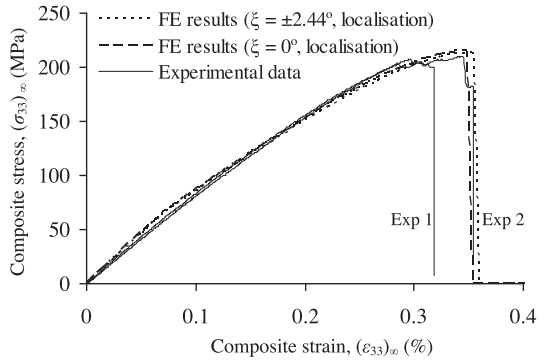

Fig. 14. Comparison of experimental stress–strain curves for the HITCO 8-Harness satin weave C/C laminate with curves predicted for $\xi = 0°$ and $\xi = \pm 2.44°$ levels of waviness and the stress–strain curve given by the model for transverse tow failure by strain controlled moduli degradation. Failure has been modelled by deformation localisation in the partial unit cell close to the weave section.

on fibre fracture by instantaneous pull-out deactivation $\varepsilon_{33} = \varepsilon_{wd} = 0.3\%$; the results are presented in Fig. 15 where they are compared with the experimental result, Exp 4.

The prediction for waviness of $\xi = \pm 2.44°$ best predict both the levels of stress and strain and also the failure strain level.

9. Discussion of results

9.1. Transverse tow failure

Comparison of the predictions the two models, i.e. transverse brittle tow failure, and transverse tow failure by strain controlled moduli degradation, are shown in Figs. 13 and 14 for zero waviness $\xi = 0°$. If failure takes place at the transverse strain of 0.07% as shown in Fig. 11c then the predictions of Fig. 13 are obtained. This results in a composite response, in the global 3-direction, that is too soft. Alternatively, if the transverse tow moduli are allowed to degrade in sympathy with the corresponding direct moduli, as defined by Eqs. (2) and (3), then acceptable predictions of Fig. 14 are obtained. If this model is correct, it infers that the amorphous carbon matrix, or the fibre–matrix interface, must degrade without the inception of a single dominant matrix crack. One possible mechanism for this is the formation of a field of continuum-type micro-cracks on a scale of the order of less than one fibre radius. However, to the knowledge of the authors, no such microscopic evidence is available; but with the advent of tomographic internal damage examination techniques this may become possible.

9.2. Fibre/tow failure by deformation localisation

The mechanism of tow failure by localisation of deformation is clearly shown in Fig. 12. As outlined in Section 8.1 failure by deformation localisation occurs when the local strain ε_{33}^{ℓ} is permitted to increase until deformation is localised in the coloured band of Fig. 12, adjacent to the weave zone, at which point the stress σ_{33}^{ℓ} across the band begins to decrease with increasing strain, then axial equilibrium can no longer be satisfied and failure ensues. This mechanism will take place in a laminate cross-section where the largest number of such events is found to take place, provided no other failure mechanism intervenes.

9.3. Dynamic fibre/tow failure by instantaneous pullout deactivation

The mechanism of dynamic fibre/tow failure by instantaneous pullout deactivation (Blacklock and Hayhurst, 2011) is probably

not triggered by a single event; this is because in the 8-Harness satin weave each straight tow zone, adjacent to a weave section, where this mechanism is first triggered has several, locally stiffer straight tows, in parallel. These tows are adjacent both in the plane of the laminate, and in the laminae above and below. It is these parallel load carrying tows that will permit stress redistribution, and will tend to negate local failure. However, a feature of the mechanism of dynamic fibre/tow failure by instantaneous pullout deactivation is that tension stress waves run along the tows and pass into adjacent unit cells, causing failure as they propagate. Other mirror-like events that may take place at distances, in both directions, further along a tow and will inevitably interact; and will make it difficult for the locally parallel straight tows to accept stable stress redistribution and hence avoid failure.

For purposes of components design it will be impossible to predict which of the two mechanisms will take place, when and where, and design will have to take place based on the most severe mechanism of dynamic fibre/tow failure by instantaneous pullout deactivation.

10. Conclusions

1. A finite-element-based multi-linear elastic approach that uses an orthotropic solid element, as a homogenised medium of a heterogeneous uni-directional tow with strain-induced damage, has been used to accurately predict the experimentally measured mechanical behaviour of the HITCO 8-Harness satin weave composites.
2. Close agreement between predictions and the results of experiments confirm the assumption that Poisson's ratio degrades linearly with strain, from the matrix crack strain to a strain associated with peak load.
3. The assumption that transverse tow failure occurs in a brittle manner, as summarised in Figs. 4 and 11, has been shown to be incapable of modelling the measured composite response of Fig. 13.
4. The assumption that transverse tow failure takes place by strain controlled moduli degradation, c.f. Eqs. (2) and (3), has been vindicated by the close agreement between predictions and experiment shown in Fig. 14. However, the postulated governing physical mechanisms require investigation and clarification.
5. It has been found necessary to introduce two classes of composite failure to accurately predict the extremes of behaviour observed in experiments i.e. quasi-ductile and brittle responses. These are:
   Either: composite failure by deformation localisation in a band that is orthogonal to the tows and passes through the weave section.
   Or: dynamic composite failure on fibre fracture by instantaneous pullout deactivation (Blacklock and Hayhurst, 2011).
   The features of the composite, or of the loading conditions, that determines which mechanism controls the behaviour are not clear, and require investigation.
6. The inter-laminar/tow properties have been assumed to be those of the amorphous carbon matrix. The good quality of predictions confirms the appropriateness of this assumption for in-plane loading of the composites.
7. The computational approach developed allows the behaviour of a composite partial unit cell to be modelled by a small number of finite elements. The high efficiency, and the simplicity of the approach, make it possible to analyse large scale woven composites; and, the use of the technique to model real engineering components will be pursued as a future development.

Acknowledgments

The authors gratefully acknowledge the financial support of: the Engineering and Physical Sciences, UK under Grant No. EP/D056276/1; and, the National Natural Science Foundation of China under Grant No. 11272207.

Appendix A. Incremental constitutive equations and material Jacobian matrix

This presentation has been given in a similar form by Zhang and Hayhurst (2010) but is presented here for completeness. For a linear elastic analysis, the constitutive equations for an orthotropic material in terms of engineering material constants are

$$\begin{Bmatrix}\sigma_{11}\\ \sigma_{22}\\ \sigma_{33}\\ \sigma_{23}\\ \sigma_{13}\\ \sigma_{12}\end{Bmatrix} = \begin{bmatrix} \frac{1-v_{23}v_{32}}{E_2E_3\Delta} & \frac{v_{21}+v_{23}v_{31}}{E_2E_3\Delta} & \frac{v_{31}+v_{21}v_{32}}{E_2E_3\Delta} & 0 & 0 & 0\\ \frac{v_{21}+v_{23}v_{31}}{E_2E_3\Delta} & \frac{1-v_{13}v_{31}}{E_1E_3\Delta} & \frac{v_{32}+v_{12}v_{31}}{E_1E_3\Delta} & 0 & 0 & 0\\ \frac{v_{31}+v_{21}v_{32}}{E_2E_3\Delta} & \frac{v_{32}+v_{12}v_{31}}{E_1E_3\Delta} & \frac{1-v_{12}v_{21}}{E_1E_2\Delta} & 0 & 0 & 0\\ 0 & 0 & 0 & G_{23} & 0 & 0\\ 0 & 0 & 0 & 0 & G_{13} & 0\\ 0 & 0 & 0 & 0 & 0 & G_{12}\end{bmatrix} \begin{Bmatrix}\varepsilon_{11}\\ \varepsilon_{22}\\ \varepsilon_{33}\\ \varepsilon_{23}\\ \varepsilon_{13}\\ \varepsilon_{12}\end{Bmatrix}, \tag{A.1}$$

where $\Delta = \frac{(1-v_{12}v_{21}-v_{23}v_{32}-v_{13}v_{31}-2v_{21}v_{32}v_{13})}{E_1E_2E_3}$ and $v_{ij} = \frac{E_i}{E_j}v_{ji}$ (i, j = 1–3 and $i \neq j$).

For a non-linear elastic analysis, the solution cannot be calculated by solving a single system of linear equations. Instead, the whole analysis is divided into many small increments; and in each increment, the analysis is approximated to that for a linear elastic problem. The stress increment for a strain increment can be calculated by using the incremental constitutive equations. Then the actual stresses are updated by adding the stress increments to the stresses at the end of the immediately previous increment.

In Eq. (A.1), all the elastic properties, E_i, v_{ij}, and G_{ij}, are constant. While the elastic properties used in the incremental constitutive equations vary, and they are functions of the strain increment. For an increment, Young's moduli and Shear moduli are the tangential slopes of their corresponding stress–strain curves, which are denoted by E_i' and G_{ij}', respectively. Due to the multi-linear discretisation, any Young's moduli and Shear moduli between two adjacent discretised points remain constant. Therefore they can be used directly in the incremental constitutive equation when the increment is within two adjacent discretised points. For Poisson's ratios, the properties linearly decrease after matrix cracking. In this situation, the Poisson's ratios at the end of an increment are used because they determine the stress state at the end of an increment.

Poisson's ratios, v_{ij}, are usually defined by the actual strains. However, for an incremental analysis, the initial state is the beginning of a strain increment rather than the actual zero strain. Hence, the incremental Poisson's ratios, v_{ij}', in the incremental constitutive equations has been calculated by the strain increment. Since the Poisson's ratios at the end of an increment are used, the relationship between the incremental Poisson's ratios, v_{ij}', and the actual Poisson's ratios, v_{ij}, at the end of an increment is derived as follows.

Fig. A.1 shows a linearly decreasing Poisson's ratio in two coordinates, where $\varepsilon_{ii} - v_{ij}$ is the coordinate of actual strain, and $\varepsilon_{ii}' - v_{ij}'$ is the coordinate of incremental strain. In both coordinate systems, the slope of the Poisson's ratio-strain curve is k_i. In the actual strain coordinate, for strain increment, $\Delta\varepsilon_{ii}$, from ε_{ii}^{bgn} to ε_{ii}^{end}, the corresponding Poisson's ratios change from v_{ij}^{bgn} to v_{ij}^{end}. The following relationships exist:

$$\varepsilon_{jj}^{bgn} = -\varepsilon_{ii}^{bgn}v_{ij}^{bgn}, \tag{A.2}$$

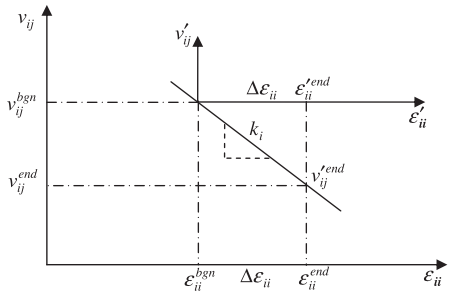

Fig. A.1. Poisson's ratios given in the coordinates of actual strains and incremental strains.

$$\varepsilon_{ij}^{end} = -\varepsilon_{ii}^{end} v_{ij}^{end}, \tag{A.3}$$

$$v_{ij}^{end} = v_{ij}^{bgn} + k_i \Delta\varepsilon_{ii}. \tag{A.4}$$

In the incremental strain coordinate, for the same strain increment, $\Delta\varepsilon_{ii}$, from 0 to ε'^{end}_{ii}, the corresponding Poisson's ratios vary from 0 to v'^{end}_{ij}. The Poisson's ratios at the end of the increment can be defined as

$$v'^{end}_{ij} = -\frac{\varepsilon'^{end}_{ij}}{\varepsilon'^{end}_{ii}}. \tag{A.5}$$

Since $\varepsilon'^{end}_{ii} = \Delta\varepsilon_{ii}$, similarly $\varepsilon'^{end}_{jj} = \Delta\varepsilon_{jj}$ can be obtained. Substitution of these expressions into Eq. (A.5) yields

$$v'^{end}_{ij} = -\frac{\Delta\varepsilon_{ij}}{\Delta\varepsilon_{ii}} = -\frac{\varepsilon_{ij}^{end} - \varepsilon_{ij}^{bgn}}{\Delta\varepsilon_{ii}}. \tag{A.6}$$

On consideration of Eqs. (A.2) and (A.3), Eq. (A.6) becomes:

$$v'^{end}_{ij} = \frac{\varepsilon_{ii}^{end} v_{ij}^{end} - \varepsilon_{ii}^{bgn} v_{ij}^{bgn}}{\Delta\varepsilon_{ii}}. \tag{A.7}$$

Substitution of $\varepsilon_{ii}^{end} = \varepsilon_{ii}^{end} + \Delta\varepsilon_{ii}$ and Eq. (A.4) into Eq. (A.7) gives:

$$v'^{end}_{ij} = v_{ij}^{bgn} + k_i\left(\varepsilon_{ii}^{bgn} + \Delta\varepsilon_{ii}\right) = v_{ij}^{bgn} + k_i\varepsilon_{ii}^{end}. \tag{A.8}$$

Finally, the incremental constitutive equations for an orthotropic material in a multi-linear elastic analysis can be expressed explicitly as:

$$\begin{Bmatrix} \Delta\sigma_{11} \\ \Delta\sigma_{22} \\ \Delta\sigma_{33} \\ \Delta\sigma_{23} \\ \Delta\sigma_{13} \\ \Delta\sigma_{12} \end{Bmatrix} = \begin{bmatrix} \frac{1-v'^{end}_{23}v'^{end}_{32}}{E'_2E'_3D} & \frac{v'^{end}_{21}+v'^{end}_{23}v'^{end}_{31}}{E'_2E'_3D} & \frac{v'^{end}_{31}+v'^{end}_{21}v'^{end}_{32}}{E'_2E'_3D} & 0 & 0 & 0 \\ \frac{v'^{end}_{21}+v'^{end}_{23}v'^{end}_{31}}{E'_2E'_3D} & \frac{1-v'^{end}_{13}v'^{end}_{31}}{E'_1E'_3D} & \frac{v'^{end}_{32}+v'^{end}_{12}v'^{end}_{31}}{E'_1E'_3D} & 0 & 0 & 0 \\ \frac{v'^{end}_{31}+v'^{end}_{21}v'^{end}_{32}}{E'_2E'_3D} & \frac{v'^{end}_{32}+v'^{end}_{12}v'^{end}_{31}}{E'_1E'_3D} & \frac{1-v'^{end}_{12}v'^{end}_{21}}{E'_1E'_2D} & 0 & 0 & 0 \\ 0 & 0 & 0 & G'_{23} & 0 & 0 \\ 0 & 0 & 0 & 0 & G'_{13} & 0 \\ 0 & 0 & 0 & 0 & 0 & G'_{12} \end{bmatrix} \begin{Bmatrix} \Delta\varepsilon_{11} \\ \Delta\varepsilon_{22} \\ \Delta\varepsilon_{33} \\ \Delta\varepsilon_{23} \\ \Delta\varepsilon_{13} \\ \Delta\varepsilon_{12} \end{Bmatrix}, \tag{A.9a}$$

where the primed values E'_i, G'_{ij}, v'_{ij} refer to the local linearised material properties, and

$$D = \frac{\left(1 - v'^{end}_{12}v'^{end}_{21} - v'^{end}_{23}v'^{end}_{32} - v'^{end}_{13}v'^{end}_{31} - 2v'^{end}_{21}v'^{end}_{32}v'^{end}_{13}\right)}{E'_1E'_2E'_3} \quad \text{and}$$

$$v'_{ij} = \frac{E'_i}{E'_j}v'_{ji} \ (i,j = 1-3 \text{ and } i \neq j),$$

or

$$\{\Delta\boldsymbol{\sigma}\} = [\mathbf{C}(\Delta\boldsymbol{\varepsilon})]\{\Delta\boldsymbol{\varepsilon}\}. \tag{A.9b}$$

The material Jacobian matrix, which is required in the ABAQUS user-defined subroutine, UMAT, is defined as $\partial\Delta\boldsymbol{\sigma}/\partial\Delta\boldsymbol{\varepsilon}$ where

$$\mathbf{d}\Delta\sigma = \frac{\partial\Delta\boldsymbol{\sigma}}{\partial\Delta\boldsymbol{\varepsilon}}\mathbf{d}\varepsilon. \tag{A.10}$$

The material Jacobian matrix can then be obtained by differentiating equation (A.9):

$$\frac{\partial\Delta\boldsymbol{\sigma}}{\partial\Delta\boldsymbol{\varepsilon}} = \frac{\partial\mathbf{C}(\Delta\varepsilon)}{\partial\Delta\boldsymbol{\varepsilon}}\Delta\boldsymbol{\varepsilon} + \mathbf{C}(\Delta\boldsymbol{\varepsilon}), \tag{A.11}$$

where

$$\frac{\partial\mathbf{C}(\Delta\varepsilon)}{\partial\Delta\boldsymbol{\varepsilon}} = \frac{\partial\mathbf{C}(\Delta\varepsilon)}{\partial v'(\Delta\boldsymbol{\varepsilon})}\frac{\partial v'(\Delta\boldsymbol{\varepsilon})}{\partial\Delta\boldsymbol{\varepsilon}}$$

$$\times \begin{bmatrix} \frac{\partial\mathbf{C}_{11}(\Delta\varepsilon)}{\partial v'(\Delta\varepsilon)}\frac{\partial v'(\Delta\varepsilon)}{\partial\Delta\boldsymbol{\varepsilon}} & \frac{\partial\mathbf{C}_{12}(\Delta\varepsilon)}{\partial v'(\Delta\varepsilon)}\frac{\partial v'(\Delta\varepsilon)}{\partial\Delta\boldsymbol{\varepsilon}} & \frac{\partial\mathbf{C}_{13}(\Delta\varepsilon)}{\partial v'(\Delta\varepsilon)}\frac{\partial v'(\Delta\varepsilon)}{\partial\Delta\boldsymbol{\varepsilon}} & 0 & 0 & 0 \\ \frac{\partial\mathbf{C}_{12}(\Delta\varepsilon)}{\partial v'(\Delta\varepsilon)}\frac{\partial v'(\Delta\varepsilon)}{\partial\Delta\boldsymbol{\varepsilon}} & \frac{\partial\mathbf{C}_{22}(\Delta\varepsilon)}{\partial v'(\Delta\varepsilon)}\frac{\partial v'(\Delta\varepsilon)}{\partial\Delta\boldsymbol{\varepsilon}} & \frac{\partial\mathbf{C}_{23}(\Delta\varepsilon)}{\partial v'(\Delta\varepsilon)}\frac{\partial v'(\Delta\varepsilon)}{\partial\Delta\boldsymbol{\varepsilon}} & 0 & 0 & 0 \\ \frac{\partial\mathbf{C}_{13}(\Delta\varepsilon)}{\partial v'(\Delta\varepsilon)}\frac{\partial v'(\Delta\varepsilon)}{\partial\Delta\boldsymbol{\varepsilon}} & \frac{\partial\mathbf{C}_{23}(\Delta\varepsilon)}{\partial v'(\Delta\varepsilon)}\frac{\partial v'(\Delta\varepsilon)}{\partial\Delta\boldsymbol{\varepsilon}} & \frac{\partial\mathbf{C}_{33}(\Delta\varepsilon)}{\partial v'(\Delta\varepsilon)}\frac{\partial v'(\Delta\varepsilon)}{\partial\Delta\boldsymbol{\varepsilon}} & 0 & 0 & 0 \\ 0 & 0 & 0 & 0 & 0 & 0 \\ 0 & 0 & 0 & 0 & 0 & 0 \\ 0 & 0 & 0 & 0 & 0 & 0 \end{bmatrix}$$

References

Blacklock, M., Hayhurst, D.R., 2011. Multi-axial failure of ceramic matrix composite fibre tows. J. Appl. Mech. 78, 031017-1–031017-10.

Blacklock, M., Hayhurst, D.R., 2012. Initial elastic properties of ceramic matrix composite fibre tows. J. Appl. Mech. 79, 051020-1–051020-11.

Blacklock, M., Bale, H., Begley, M.R., Cox, B.N., 2012. Generating virtual textile composite specimens using statistical data from micro-computed tomography: 1D tow representations for the binary model. J. Mech. Phys. Solids 60 (3), 451–470.

Bordeu, F., Boucard, P.A., Lubineau, G., 2010. A mesoscale model for damage, cracking and delamination prediction in composite materials. Sci. Eng. Compos. Mater. 17 (4), 271–282.

Burr, A., Hild, F., Leckie, F.A., 1997. Continuum description of damage in ceramic-matrix composites. Eur. J. Mech. A/Solids 16, 53–78.

Dasgupta, A., Agarwal, R.K., 1992. Orthotropic thermal conductivity of plain-weave fabric composites using a homogenization technique. J. Compos. Mater. 26, 2736–2758.

Evans, A.G., Naslain, R., 1995. High-temperature ceramic-matrix composites. Ceram. Trans. 57, 381–388.

Flores, S., Evans, A.G., Zok, F.W., Genet, M., Cox, B.N., Marshall, D., Sudre, O., Yang, Q.D., 2010. Treating matrix nonlinearity in the binary model formulation for 3D ceramic composite structures. Compos. A 41, 222–229.

Hayhurst, D.R., 2013. Numerical analysis of the coupling between mechanical strain and thermal conductivity of ceramic matrix composites', keynote lecture. In: Idelsohn, S., Papadrakakis, M., Schrefler, B. (Eds.), Proceedings of V International Conference on Computational Methods for Coupled Problems in Science and Eng. 17–19 June 2013, Sta. Eulalia, Ibiza, Spain, first ed., CD-Publication, International Centre for Numerical Methods in Engineering, Barcelona, Spain, pp. 432–444. Depósito legal: B-14078-2013 ISBN: 978-84-941407-6-1.

Hayhurst, D.R., Leckie, F.A., Evans, A., 1991. Component design-based model for deformation and rupture of tough fibre-reinforced ceramic matrix composites. Proc. R. Soc. Lond. A 434, 369–381.

Ismar, H., Schroter, F., Streicher, F., 2000. Modeling and numerical simulation of the mechanical behavior of woven SiC/SiC regarding a three-dimensional unit cell. Comput. Mater. Sci. 19, 320–328.

Karandikar, P., Chou, T., 1993. Characterization and modelling of microcracking and elastic moduli changes in Nicalon/CAS composites. Compos. Sci. Technol. 46, 253–263.

Kuhn, J.L., Charalambides, P.G., 1998. Elastic response of porous matrix plain weave fabric composite: Part I-modeling. J. Compos. Mater. 23 (16), 1426–1471.

Ladeveze, P., Lubineau, G., 2003. On a damage mesomodel for laminates: micromechanics basis and improvement. Mech. Mater. 35 (8), 763–775.

Lubineau, G., 2010. A pyramidal modeling scheme for laminates – identification of transverse cracking. Int. J. Damage Mech. 19 (4), 499–518.

Lubineau, G., Ladevèze, P., 2008. Construction of a micromechanics-based intralaminar mesomodel, and illustrations in ABAQUS/standard. Comput. Mater. Sci. 43, 137–145.

Marshall, D.B., Cox, B.N., 2008. Integral textile ceramic structures. Annu. Rev. Mater. Res. 38, 425–443.

McGlockton, M.A., Cox, B.N., McMeeking, R.M., 2003. A binary model of textile composites: III high failure strain and work of fracture in 3D weaves. Acta Metall. Mater. 51, 1573-16.

Onal, L., Adanur, S., 2007. Modeling of elastic, thermal, and strength/failure analysis of tow-dimensional woven composites–a review. Appl. Mech. Rev. Trans. ASME 60, 37–49.

Rinaldi, R.G., Blacklock, M., Bale, H., Begley, M.R., Cox, B.N., 2012. Generating virtual textile composite specimens using statistical data from micro-computed tomography: 3D tow representations. J. Mech. Phys. Solids 60 (8), 1561–1581.

Sheikh, M.A., Taylor, S.C., Hayhurst, D.R., Taylor, R., 2001. Microstructural finite element modelling of a ceramic matrix composite to predict experimental measurements of its macro thermal properties. Model. Simul. Mater. Sci. Eng. 9, 7–23.

Sheikh, M.A., Taylor, S.C., Hayhurst, D.R., Taylor, R., 2009. Experimental investigation of the effect of mechanical loading on thermal transport in ceramic matrix composites. J. Multiscale Model. 1 (3–4), 403–433.

SIMULIA, 2008. ABAQUS user's manual. Version 6.8. Providence, Rhode Island, US.

Tan, P., Tong, L., Steven, G.P., 1997. Modelling for predicting the mechanical properties of textile composites–a review. Compos. A 28A, 903–922.

Tan, P., Tong, L., Steven, G.P., 1999. Micromechanics models for the elastic constants and failure strengths of plain weave composites. Compos. Struct. 47, 797–804.

Tang, C., Hayhurst, D.R., 2011. Predictions of thermo-mechanical behaviour of a Nicalon-CAS 0°–90° ceramic matrix composite from constituent materials properties'. J. Compos. Mater. 45 (12), 1337–1350.

Tang, C., Blacklock, M., Hayhurst, D.R., 2009. Uni-axial stress-strain response and thermal conductivity degradation of ceramic matrix composite fibre tows. Proc. R. Soc. A 465, 2849–2876.

Tang, C., Blacklock, M., Hayhurst, D.R., 2011a. Stress–strain response and thermal conductivity degradation of ceramic matrix composite fibre tows in 0°–90° uni-directional and woven composites'. J. Compos. Mater. 45 (14), 1461–1482.

Tang, C., Sheikh, M.A., Hayhurst, D.R., 2011b. Finite element modelling of transverse deformation in representative volume elements of ceramic matrix composites (CMCs). J Multiscale Model. 2 (1–2), 107–126.

Tanov, R., Tabiei, A., 2001. Computationally efficient micromechanical models for woven fabric composite elastic moduli. J. Appl. Mech. 68, 553–560.

Woo, K., Whitcomb, J.D., 1997. Effects of fiber tow misalignment on the engineering properties of plain weave textile composites. Compos. Struct. 37, 343–355.

Xu, J., Cox, B.N., McGlockton, M.A., Carter, W.C., 1995. A binary model of textile composites–II. The elastic regime. Acta Metall. Mater. 43, 3511–3524.

Yang, Q.D., Cox, B.N., 2003. Spatially averaged local strain in textile composites via the binary model formulation. J. Eng. Mater. Technol. Trans. ASME 125, 418–425.

Yang, Q.D., Cox, B.N., 2010. Predicting failure in textile composites using the binary model with gauge-averaging. Eng. Fract. Mech. 77, 3174–3189.

Zhang, Y., Harding, J., 1990. A numerical micromechanics analysis of the mechanical properties of a plain weave composite. Comput. Struct. 36 (5), 839–844.

Zhang, D., Hayhurst, D.R., 2009. A finite element model to predict multi-axial stress strain response of ceramic matrix composites with strain induced damage. In: The 17th International Conference on Composite Materials, July 2009, Edinburgh.

Zhang, D., Hayhurst, D.R., 2010. Stress–strain and fracture behaviour of 0°/90° and plain weave ceramic matrix composites from tow multi-axial properties. Int. J. Solids Struct. 47, 2958–2969.

Zhang, D., Hayhurst, D.R., 2011. Influence of applied in-plane strain on transverse thermal conductivity of 0°/90° and plain weave ceramic matrix composites. Int. J. Solids Struct. 48 (5), 828–842.